Investigation of Ga interstitial and vacancy diffusion in β-Ga_2O_3 via split defects: A direct approach via master diffusion equations

Channyung Lee [1], Michael A. Scarpulla [2], and Elif Ertekin [1,3,*]

[1]*Department of Mechanical Science and Engineering, University of Illinois at Urbana-Champaign, 1206 W. Green Street, Urbana, Illinois 61801, USA*

[2]*Department of Materials Science and Engineering, University of Utah, Salt Lake City, Utah 84112, USA*

[3]*Materials Research Laboratory, University of Illinois at Urbana-Champaign, Urbana, Illinois 61801, USA*

(Received 15 February 2024; accepted 30 April 2024; published 13 May 2024)

The low symmetry of monoclinic β-Ga_2O_3 leads to elaborate intrinsic defects, such as Ga vacancies split amongst multiple lattice sites. These defects contribute to fast, anisotropic Ga diffusion, yet their complexity makes it challenging to understand dominant diffusion mechanisms. Here, we predict the 3D diffusivity tensors for Ga interstitials (Ga_i^{3+}) and vacancies (V_{Ga}^{3-}) via first principles and direct solution of the master diffusion equations. We first explore the maximum extent of configurationally complex "*N*-split" Ga interstitials and vacancies. With dominant low-energy defects identified, we enumerate all possible elementary hops connecting defect configurations to each other, including interstitialcy hops. Hopping barriers are obtained from nudged elastic band simulations. Finally, the comprehensive sets of (i) defect configurations and their energies and (ii) the hopping barriers that connect them are used to construct the master diffusion equations for both Ga_i^{3+} and V_{Ga}^{3-}. The solution to these equations yields the Onsager transport coefficients, i.e., the components of the 3D diffusivity tensors D_{Ga_i} and $D_{V_{Ga}}$ for Ga_i^{3+} and V_{Ga}^{3-}, respectively. It further reveals the active diffusion paths along all crystallographic directions. We find that both Ga_i^{3+} and V_{Ga}^{3-} diffusion are fastest along the *c* axis, due to three-split defects that bridge neighboring unit cells along the *c* axis and enable diffusing species to circumvent pathways with high-energy migration barriers. Although isolated Ga_i^{3+} diffuse faster than isolated V_{Ga}^{3-}, self-diffusion of Ga is predominantly mediated by V_{Ga}^{3-} due to the higher V_{Ga}^{3-} defect concentration under most thermodynamic environments.

DOI: 10.1103/PhysRevMaterials.8.054603

I. INTRODUCTION

The growing demand for power electronics requires the exploration of new semiconductor materials to effectively meet increasing needs for performance. Monoclinic gallium oxide (β-Ga_2O_3) is a notable candidate due to its unique properties, including an ultrawide band gap (~4.8 eV), high breakdown voltage (~8 MV/cm), and tunable *n*-type conductivity [1–4]. Additionally, the availability of β-Ga_2O_3 in high-quality single crystal wafers and epitaxial thin films enhances its appeal for device fabrication and characterization [5–7].

An understanding of the migration mechanisms of intrinsic defects is essential to exploit the potential of β-Ga_2O_3 in practical applications. The self-diffusion of Ga cations, for example, is mediated by Ga interstitials (Ga_i) and vacancies (V_{Ga}), and is a fundamental mechanism for mass transport within β-Ga_2O_3. Ga_i and V_{Ga} native defects also can serve as vehicles for dopant diffusion, including shallow donors such as Si_{Ga} and Sn_{Ga}, as well as deep compensating acceptors like Mg_{Ga} and Fe_{Ga} [8–12]. Investigating migration mechanisms of Ga_i and V_{Ga} could lead to precise control over dopant distributions, enabling the tailoring of properties to improve performance and stability. Additionally, investigating transport mechanisms also helps elucidate degradation pathways like electromigration.

The low symmetry of monoclinic β-Ga_2O_3 leads to many interesting complexes of intrinsic defects, such as Ga vacancies split between two or three neighboring Ga sites. These 2, 3, and "*N*"-split defects ($N = 2, 3, 4, ...$), many of which have been observed experimentally, are expected to contribute to fast and anisotropic ion diffusion in β-Ga_2O_3, posing challenges for understanding dominant diffusion mechanisms [13–19]. Previous computational studies, including a recent extensive analysis by Frodason *et al.* [11], have explored migration pathways involving split defects. Yet, there remains an opportunity to fully elucidate the 3D diffusion network for both Ga_i and V_{Ga}. A quantitative analysis of the diffusivity tensors D_{Ga_i} and $D_{V_{Ga}}$, accounting for contributions from the full spectrum of intrinsic defects, would provide microscopic insights into defect migration pathways, diffusion anisotropy, and related processes like material degradation. Knowledge of the full diffusivity tensor obtained from first-principles may lead to predictions amenable to experimental validation.

In this study, we use first-principles calculations and a direct approach based on the solution of the master diffusion equations to determine the 3D diffusion tensors for Ga_i^{3+} and V_{Ga}^{3-}, interstitials and vacancies in their dominant charge

*Corresponding author: ertekin@illinois.edu

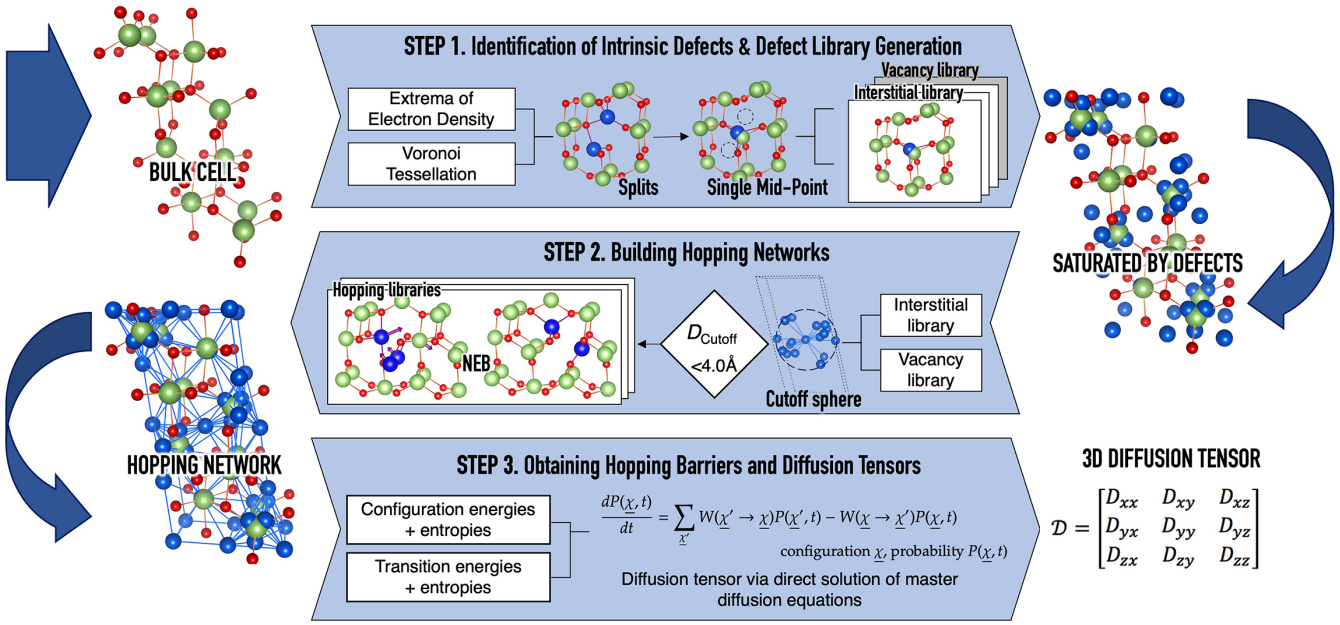

FIG. 1. Schematic representation of the workflow used in this work to obtain the diffusivity tensors for vacancy and interstitial defects in β-Ga_2O_3. The approach is based on assembling and solving the master diffusion equations via the Onsager methodology [20–22].

state in β-Ga_2O_3. We first explore a wide range of defects, including N-split defects, and analyze (i) their formation energies and (ii) the migration barriers for hops connecting one defect to another. The analysis includes the identification of 32 unique interstitial and interstialcy hops between 20 different configurations of Ga interstitials, and 31 unique vacancy hops between 19 different configurations of Ga vacancies. By combining defect configuration energies and hopping barriers, we construct the master diffusion equations for both Ga_i^{3+} and V_{Ga}^{3-} [20–22]. Solving these equations yields the Onsager transport coefficients in the form of 3D diffusivity tensors D_{Ga_i} and $D_{V_{Ga}}$. We find that both Ga interstitials and Ga vacancies exhibit the highest diffusivity along the c axis, and that the components of the interstitial diffusivity tensor D_{Ga_i} are larger than those of vacancy diffusivity tensor $D_{V_{Ga}}$. However, Ga self-diffusion is predicted to still be mediated by V_{Ga}^{3-} rather than Ga_i^{3+}, due to the higher concentration of vacancies under typical environments. These findings are relevant to the design and optimization of β-Ga_2O_3 electronics.

II. METHODS

A. Master diffusion equations

For assembling and then solving the master diffusion equations, we used the Onsager software package [20–22], which yields the components of the diffusivity tensor. We implement the method separately for interstitial diffusion and vacancy diffusion, and obtain isolated diffusion tensors D_{Ga_i} and $D_{V_{Ga}}$ respectively, for each mechanism. Hence, we construct two independent diffusion networks, one for interstitials and the other for vacancies. The overall methodology consists of three stages, as illustrated in Fig. 1.

In the first stage (Fig. 1, step 1), defect libraries are generated by identifying possible atomic configurations of Ga_i^{3+} and V_{Ga}^{3-} and determining their formation energies (site energies) as described below. The defect library includes extended defect complexes such as N-split Ga_i^{3+} formed by combinations of N interstitials and (N-1) vacancies, and N-split V_{Ga}^{3-} formed by combinations of N vacancies and (N-1) interstitials. For instance, a four-split Ga_i^{3+} comprises four distinct Ga interstitials and three Ga vacancies, while a four-split V_{Ga}^{3-} consists of four Ga vacancies and three Ga interstitials. N-split Ga_i^{3+} and N-split V_{Ga}^{3-}, respectively introduce an extra Ga or a missing Ga, resulting in a defect that is spread across multiple lattice sites instead of at a single lattice point (details in Fig. S1 [23]). In the defect library, we employ a single representative mid-point located in the middle of a given N-split defect to represent the position of each N-split defect, facilitating the tracking of transitions between extensive N-split configurations and accommodating interstitialcy hopping.

In the second stage (Fig. 1, step 2), the complete hopping network is assembled. All symmetry-unique interstitial-to-interstitial hops (for the interstitial diffusion network) and vacancy-to-vacancy hops (for the vacancy network), lying within a 4 Å cutoff distance, are enumerated. We then obtain migration barriers for these hops using the climbing image-nudged elastic band (CI-NEB, see below). The library of defect configurations (and associated site energies) and the library of hops (and associated transition rates) that connect different configurations to each other form the three-dimensional diffusion network for each mechanism.

In the final stage (Fig. 1, step 3), the identified diffusion pathways, site energies, and transition rates are assembled into a system of coupled rate equations. The formulation is based on the Onsager reciprocal relations that express the linear relationship between generalized fluxes and forces in thermodynamic systems. The constants of proportionality (the Onsager coefficients) are the diffusivities. The Onsager formulation relies on the assumption of well-defined

configurations χ that thermalize faster than transitions occur. Diffusion is considered as a Markov process consisting of transitions from one state χ to another χ'. The quantity $P(\chi, t)$ denotes the probability of finding the system in state χ at time t. As indicated in Fig. 1, step 3, the time rate of change is given by

$$\frac{dP(\chi,t)}{dt} = \sum_{\chi'} (W(\chi' \to \chi)P(\chi',t) - W(\chi \to \chi')P(\chi,t)), \tag{1}$$

involving a sum over transition rates $W(\chi' \to \chi)$ from all other configurations χ' into configuration χ and a sum over transition rates $W(\chi \to \chi')$ from configuration χ into all other configurations χ'. Under thermodynamic equilibrium where $P(\chi, t)$ is fixed, the system of equations above (one for each configuration χ) can be solved under the constraint of detailed balance. By assembling and self-consistently solving the system, we obtain the linear transport coefficients $D_{\mathrm{Ga_i^{3+}}}$ and $D_{\mathrm{V_{Ga}^{3-}}}$, the diffusivity tensors for isolated $\mathrm{Ga_i^{3+}}$ and $\mathrm{V_{Ga}^{3-}}$, respectively. Finally, self-diffusion coefficients for Ga, labeled $D_{\mathrm{Self,Ga_i^{3+}}}$ and $D_{\mathrm{SelfV_{Ga}^{3-}}}$ respectively for interstitials and vacancies, are obtained using jump balance. A more detailed description of the approach is given in Refs. [20–22]; for completeness a brief discussion is presented in Appendix A.

B. Site energies and migration barriers

To obtain site energies and migration barriers, we used first-principles simulations. All first-principles simulations were performed using density functional theory [24,25] with the projector augmented wave (PAW) method [26,27] as implemented in the Vienna *ab initio* simulation package (VASP) [28,29]. The Perdew-Burke-Ernzerhof (PBE) [30] parametrization of the generalized gradient approximation (GGA) [31] was used to describe the exchange-correlation functional. The plane-wave basis cutoff was set at 420 eV, and Ga $3d$ electrons were explicitly included as valence states in the chosen pseudopotentials. For geometry optimization, the convergence criteria were set at 1×10^{-6} eV for energy and 0.001 eV/Å for the residual forces on each atom. The ground-state lattice parameters of the monoclinic β-Ga_2O_3 conventional unit cell were determined to be $a =$ 12.47 Å, $b = 3.09$ Å, $c = 5.88$ Å, and $\beta = 103.7^\circ$ These values agree well with previously reported results obtained using PBE functionals [14,32,33] and experimental measurements [34,35].

The focus of this work is on the 3+ charge state of $\mathrm{Ga_i}$ and the 3− charge state of $\mathrm{V_{Ga}}$, the stable charge state for each defect under typical n-type doping or unintentionally doped conditions in β-Ga_2O_3. Defect formation energies (site energies) were obtained using the usual supercell formulation, as described in Appendix B. To accurately describe the extended N-split defects when determining their formation energies, we employed different supercell sizes at different stages of the study. In the initial stage, we utilized 160 atoms in $1 \times 4 \times 2$ supercells to comprehensively screen and identify all potential defective configurations which we assembled from multiple sources. The configurations analyzed include simple point interstitials obtained through both Voronoi tessellations [36] and electron density topology analysis [15], as well as new N-split defects constructed manually and designed based on generalization of previously reported two- or three-split defects [14,16,17]. In total, we considered 27 unique $\mathrm{Ga_i}$ structures and 25 unique $\mathrm{V_{Ga}}$ structures. After excluding the highest energy structures, we used $1 \times 4 \times 3$ supercells with 240 atoms and $2 \times 4 \times 2$ supercells with 320 atoms to minimize finite size effects from the extended nature of N-split defects along the c and a axes, respectively. A $2 \times 2 \times 2$ k-point grid generated by the Monkhorst-Pack method was used for all supercells [37].

Migration barriers were calculated using the climbing-image nudged elastic band [38] with a 0.1 eV/Å convergence criterion for the residual forces on each atom. Considering the computational cost of NEB calculations, for a given defect we selected one from four different possible supercell sizes ($1 \times 4 \times 2$, $1 \times 4 \times 3$, $2 \times 4 \times 2$, and $2 \times 4 \times 3$) based on the crystal directions along which starting and ending structures are most extended, again to minimize finite size effects.

To account for uncertainties in estimated migration barriers arising from the choice of PBE for the DFT exchange correlation functional, we benchmarked the current PBE migration barriers using $1 \times 4 \times 2$ and $1 \times 4 \times 3$ supercells against the results from Frodason *et al.* [17], who employed both the strongly constrained and appropriately normed (SCAN) [39] and Heyd-Scuseria-Ernzerhof (HSE) [40,41] functionals. This comparison revealed a mean discrepancy of 0.085 eV for the current PBE results and their HSE-calculated barriers, as shown in Fig. S8 [23]. This discrepancy is similar to the differences between SCAN and HSE reported by Frodason *et al.* suggesting that PBE and SCAN give similar barriers for this material system. Therefore, in the forthcoming results, we show predicted diffusivities in a range of values accounting for a ±0.1 eV uncertainty for all migration barriers.

III. RESULTS AND DISCUSSION

A. Defect configurations and formation energies

Previous theoretical studies have revealed diverse ranges of energetically stable defect complexes in β-Ga_2O_3. Therefore our first objective was to systematically explore and identify as many as stable defect structures in β-Ga_2O_3 as possible, including extended defects. We tested numerous combinations of split defect structures by further splitting along the ac plane. We carefully selected initial defect configurations to ensure they are close to the final target configurations, and following relaxation we carefully categorized the resulting geometry into the appropriate N-split defects. This approach was motivated by previous theoretical findings that the tetrahedral $\mathrm{Ga_{(I)}}$ atoms may shift towards the center of the b-axis channels through the formation of stable octahedral or tetrahedral Ga-O bonds [16–18]. This shift induces the formation of split defects such as $\mathrm{Ga_i}$-$\mathrm{V_{Ga}}$-$\mathrm{Ga_i}$ two-split interstitials (comprising two interstitials and one vacancy) or $\mathrm{V_{Ga}}$-$\mathrm{Ga_i}$-$\mathrm{V_{Ga}}$ two-split vacancies (comprising two vacancies and one interstitial), and possibly further extended defects on larger scales. Specifically, the rearrangement of multiple $\mathrm{Ga_{(I)}}$ atoms allows for the formation of continuous defect chains consisting of N vacancies and (N-1) interstitials (or vice versa). Through our

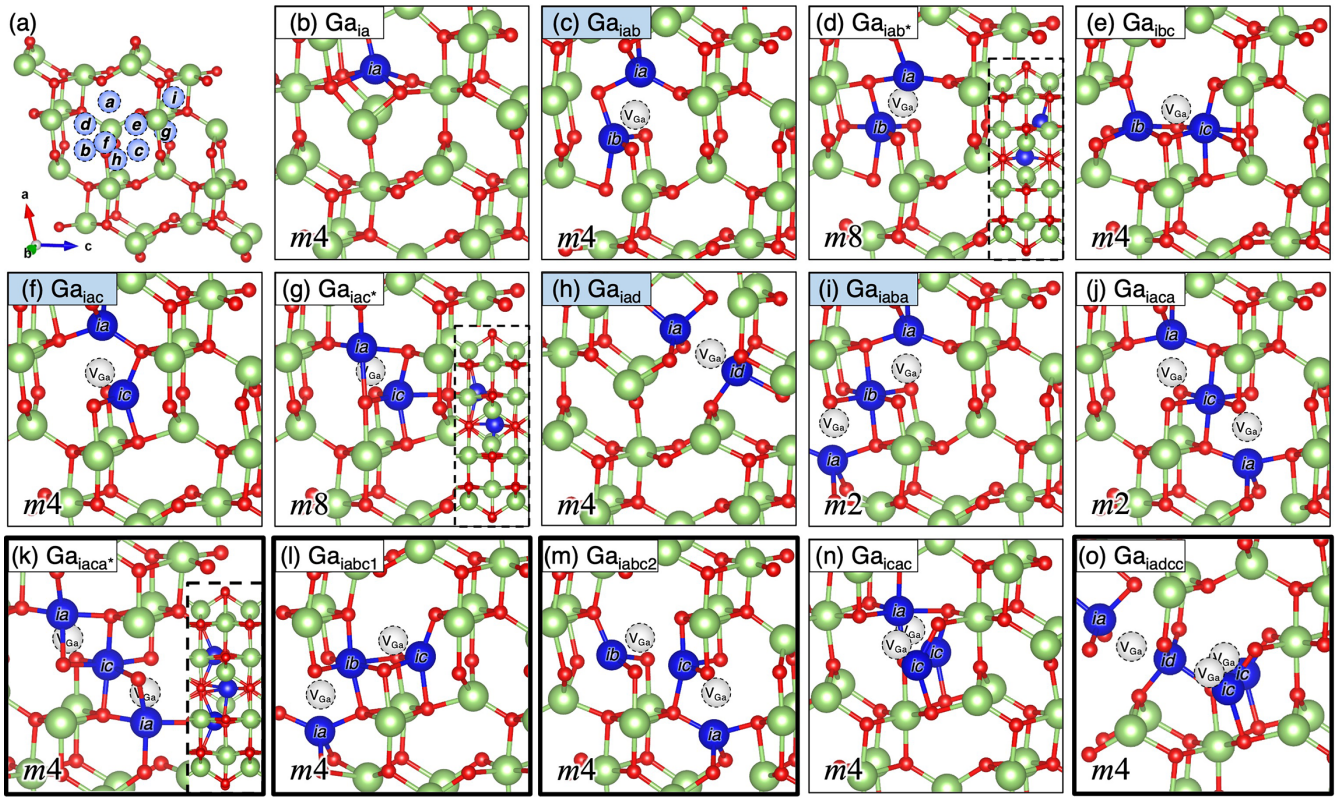

FIG. 2. (a) Monoclinic β-Ga_2O_3 structure, highlighting unique Ga interstitial sites (*a*-*i*). A series of relaxed defective β-Ga_2O_3 structures with selected Ga_i^{3+} defects including (b) a single interstitial, [(c)–(h)] two-split interstitials, [(i)–(n)] three-split interstitials, and (o) a four-split interstitial. Split Ga interstitials are represented by blue spheres, and Ga vacancies by gray spheres. The letter *m* in the lower left corner denotes "multiplicity," and the following integer indicates the defect site multiplicity imposed by symmetry. The newly identified structures are indicated by a bold outline. Name boxes colored in blue are used to indicate the four structures with the lowest energy. The interstitials shown are the ones predicted to contribute to interstitial-mediated diffusion.

exploration, we identified a total of 25 distinct Ga_i^{3+} configurations, ranging from single-point interstitials to four-split interstitials, and a total of 27 distinct V_{Ga}^{3-} configurations, ranging from single-point vacancies to four-split vacancies.

To facilitate structural characterization of a wide range of defect complexes, here onwards we employ a simplified notation (*a*-*i*) to label the unique possible lattice sites for Ga atoms in the β-Ga_2O_3 unit cell, as depicted in Fig. 2(a). The sites are illustrated from the *b*-axis channel viewing direction, which we found to be the easiest direction to observe the configurations. The lattice site located in the large eight-sided channel (A channel) is denoted as *a*, while the sites positioned in the two irregular hexagonal channels (B and C channels) are labeled as *b* and *c*, according to established conventions [11,18]. Additionally, the lattice sites located between the tetrahedral $Ga_{(I)}$ and the hexagonal $Ga_{(II)}$ are denoted as *d* and *e*, while those located between two tetrahedral $Ga_{(I)}$ and between two hexagonal $Ga_{(II)}$ along the *b* axis are labeled as *f* and *g*, respectively. These notations for lattice sites are used to describe both *N*-split interstitials and *N*-split vacancies.

1. Ga interstitial configurations

The main interstitial Ga_i^{3+} configurations that we ultimately find to be responsible for the formation of the major diffusion pathways along each of the three different crystal orientations (a^*, *b*, and *c*) are shown in Figs. 2(b)–2(o); the additional configurations considered can be found in Fig. S2 [23]. The newly identified structures are indicated by a bold outline, while the four structures with the lowest energies are highlighted by blue-colored name boxes. First, we investigated three distinct configurations of single interstitials positioned in the A, B, and C channels. The structure of Ga_{ia} in the A channel, as shown in Fig. 2(b), exhibits stable pyramidal Ga-O bonds. On the other hand, Ga_{ib} and Ga_{ic}, located in the B and C channels, respectively [shown in Figs. S2(a) and S2(b) [23]], form octahedral Ga-O bonds by attracting four neighboring threefold oxygen atoms (O_{ii} and O_i, respectively) towards the central Ga interstitial, resulting in significantly higher energies compared to Ga_{ia}.

For N-split interstitials, we identified unique combinations of *N* interstitials split into multiple sites (*a*-*g*) and the corresponding host (*N*-1) Ga vacancies that arise when simple interstitials shift. Regarding two-split interstitials, we identified a total of eight distinct structures. The two-split interstitials Ga_{iab}, Ga_{ibc}, and Ga_{iac} [Figs. 2(c), 2(e), and 2(f)] exhibit Ga_i-V_{Ga}-Ga_i structures, where two interstitials are positioned in three distinct channels sharing one $V_{Ga(I)}$ site. We also tested another configuration, Ga_{iah} (Fig. S2(d) [23]), in which the interstitial is split between site *a*, and, at a location halfway between B and C channels. However, this configuration was found to have an energy of more than 1 eV

higher than the others. Additionally, we explored other sets of two-split interstitials denoted as Ga_{iad} and Ga_{iei} [Fig. 2(h) and S2(c), [23] respectively], which share the $V_{Ga(II)}$ site and for which the two Ga_i form tetrahedral bonds in different orientations. However, the presence of an interstitial atom in the small rhombohedral channel in Ga_{iei} significantly distorts the lattice, resulting in high energy compared to Ga_{iad}. Among the investigated two-split structures, the Ga_{iac} configuration exhibited the lowest formation energy, while Ga_{iad} showed the second lowest. During NEB calculations of *b*-axis hops involving Ga_{iab} and Ga_{iac}, we discovered two additional non-symmetric structures along the *b* axis, denoted Ga_{iab^*} and Ga_{iac^*} [Figs. 2(d) and 2(g)]. In these structures, the interstitials Ga_{ia} exhibit slight displacements from the *ac* plane where the $V_{Ga(I)}$ is located, compared to the corresponding symmetric structures of Ga_{iab} and Ga_{iac} shown in Figs. 2(d) and 2(g), respectively.

We further identified 15 unique configurations of three-split interstitials. These were constructed by associating pairs of two nearby Ga vacancies with three neighboring Ga interstitials: one situated between the two vacancies and the others adjacent to each vacancy. From the $V_{Ga(I)}$-$V_{Ga(I)}$ pair centered on channel B of the *ac* plane, we identified Ga_{iaba}, Ga_{icbc}, and Ga_{iabc1} [Figs. 2(i), 2(l), and S2(i) [23], respectively]. In the $V_{Ga(I)}$-$V_{Ga(I)}$ set centered in the C channel in the *ac* plane, we found Ga_{iaca}, Ga_{ibcb}, and Ga_{iabc2} [Figs. 2(j), 2(m), and S2(h) [23], respectively]. Although previous studies often categorize Ga_{iaba} and Ga_{iaca} as point interstitials [17], we classified these configurations as three-split interstitials because the two shifted interstitial atoms from Ga(I) sites form stable tetrahedral bonds in different A channels, deviating from the original hexagonal channels. Along the *b* axis, the $V_{Ga(I)}$-$V_{Ga(I)}$ set yielded Ga_{icac} and Ga_{ibab} [Figs. 2(n) and S2(k) [23], respectively]. In the $V_{Ga(I)}$-$V_{Ga(II)}$ set, we identified Ga_{iadc} and Ga_{iaha} [Figs. S2(j) and S2(m) [23]]. Ga_{ieie} was identified in the $V_{Ga(I)}$-$V_{Ga(I)}$ set [Fig. S2(l) [23]]. We were able to identify additional off-symmetric structures along the *b* axis for three-split interstitials, specifically derived from Ga_{iaba} and Ga_{iaca}. These additional structures, labeled Ga_{iaba^*}, $Ga_{iaba^{**}}$, Ga_{iaca^*}, and $Ga_{iaba^{**}}$ [Figs. S2(e), S2(f), 2(k), and S2(g) [23], respectively], exhibit shifted *ia* split interstitials along the *b* axis, deviating from the *ac* plane where the *ia* and *ib* interstitials are located along with two $V_{Ga(I)}$'s, respectively. Lastly, we identifed only one four-split interstitial, Ga_{iadcc} [Fig. 2(o)], which exhibits a structure similar to Ga_{iadc} and Ga_{icac}. Due to the increased size of the defect cluster and resulting complexities, we were unable to extensively explore further four-split interstitials.

After excluding high-energy structures based on a cutoff of 1 eV for relative formation energies, referenced to the lowest energy structure of Ga_{iac} as shown in Fig. S4(a) [23], we increased the size of the supercells to accurately capture the extended nature of the *N*-split interstitials. As a specific example, in the well-known Ga interstitial structures of Ga_{iaba} and Ga_{iaca}, as shown in Figs. 2(i) and 2(j), respectively, the split interstitial chains extend along the *a* axis and interact directly with neighboring supercells above and below simultaneously. Under $1 \times 4 \times 2$ supercells, this interaction leads to spurious lattice distortions at the supercell boundary as two Ga(II) atoms shift toward the center of the lattice, resulting in high strain energy under periodic boundary conditions. Therefore we reoptimized low-energy Ga_i^{3+} structures and recalculated their formation energies using $1 \times 4 \times 3$ and $2 \times 4 \times 2$ supercells [Fig. S4(b) [23]].

When expanding the supercells, for single interstitial Ga_{ia}, there were no noticeable differences in the formation energies. However, substantial formation energy variations were observed for *N*-split Ga interstitials depending on the supercell size, emphasizing the importance of selecting the appropriate supercell according to the direction of extension. In $2 \times 4 \times 2$ supercells, the formation energies of Ga_{iab}, Ga_{iac}, Ga_{iad} decreased by approximately 0.1 eV each and those of Ga_{iaba} and Ga_{iaca} decreased by approximately 0.4 eV each when adequate spacing was included between defect clusters or chains. In particular, significant energy differences were observed in Ga_{iaba} and Ga_{iaca}, suggesting that their stability may have been underestimated due to finite size effects in previous theoretical calculations using conventional $1 \times 4 \times 2$ supercells. Similarly, using $1 \times 4 \times 3$ supercells, the formation energies of Ga_{ibc} and Ga_{iadcc} decreased by approximately 0.15 eV each and those of Ga_{ibcb} and Ga_{icbc} decreased by approximately 0.4 eV each due to sufficient spacing between defect clusters along the *c* axis.

2. Ga vacancy configurations

Figure 3 illustrates the relaxed V_{Ga}^{3-} structures, including point vacancies and *N*-split vacancies ultimately found to be important for vacancy diffusion. As before, newly identified structures are indicated by a bold outline, while the four structures with the lowest energies are highlighted by blue-colored name boxes. Consistent with previous studies, the formation energy of $V_{Ga(I)}$ was found to be higher than $V_{Ga(II)}$ [Figs. 3(a) and 3(b)], indicating that $V_{Ga(I)}$ serves as the more stable split vacancy center. To identify two-split vacancies, we followed a similar approach used in the identification of *N*-split interstitials, examining V_{Ga}-V_{Ga} sets and placing an interstitial between two vacancies. A total of seven distinct two-split vacancies were identified from each V_{Ga}-V_{Ga} arrangement. In the *ac* plane, three different two-split vacancies (V_{Ga}^{ia}, V_{Ga}^{ib}, and V_{Ga}^{ic}) as illustrated in Figs. 3(c)–3(e) showed lower formation energies than the other off *ac*-plane two-split vacancies, such as V_{Ga}^{ie}, V_{Ga}^{ig}, V_{Ga}^{id}, and V_{Ga}^{if} [Figs. 3(f), 3(g) and S4(a), S4(b) [23], respectively]. To identify *N*-split vacancies where $N \geqslant 3$, we employed a more straightforward method based on the identified two-split vacancies. This method involved coupling two adjacent low-energy two-split vacancies ($V_{Ga}Ga_iV_{Ga}^* + V_{Ga}^*Ga_iV_{Ga}$) in such a way that they share one vacancy site V_{Ga}^*, resulting in another split vacancy of $V_{Ga}Ga_iV_{Ga}^*Ga_iV_{Ga}$. This strategy enabled us to create extended chains of $(V_{Ga}Ga_i)_nV_{Ga}$, representing continuous sequences of *N*-split vacancies. As a result, we identified seven and nine unique triple and quadruple splits, respectively.

To mitigate finite-size effects, we again employed larger supercells, $1 \times 4 \times 3$ and $2 \times 4 \times 2$, to reoptimize the low-energy V_{Ga}^{3-} structures we identified. As depicted in Fig. S5 [23], no significant differences are observed in the formation energies of the point vacancies and the two-split vacancies. This finding can be attributed to the small size of the two-split vacancy clusters, which results from the localized lattice

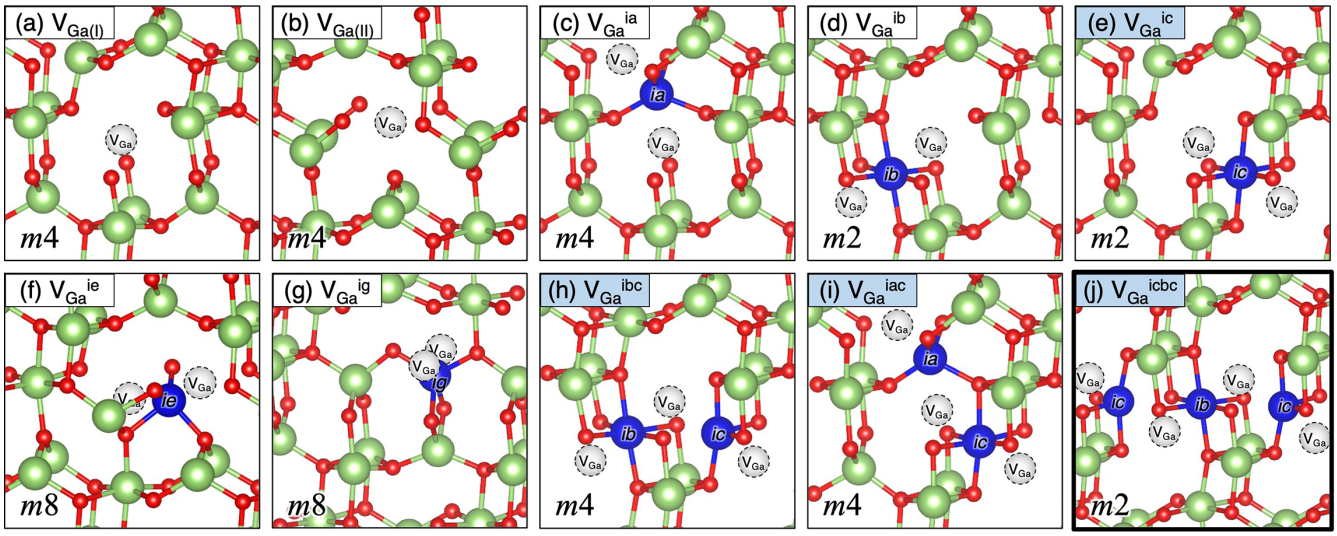

FIG. 3. Relaxed defective β-Ga_2O_3 structures with selected V_{Ga}^{3-} defects including [(a) and (b)] single-point vacancies, [(c)–(g)] two-split vacancies, [(h) and (i)] three-split vacancies, and (j) a four-split vacancy. Split Ga interstitials are represented by blue spheres, and Ga vacancies by gray spheres. The letter "m" in the lower left corner denotes "multiplicity," and the following integer indicates the defect site multiplicity imposed by symmetry. The newly identified structures are indicated by a bold outline. Name boxes colored in blue are used to indicate the four structures with the lowest energy. The vacancies shown are the ones predicted to contribute to vacancy-mediated diffusion.

distortion caused by the vacancies and the confined interstitial within the clusters.

In contrast, we observed substantial variations in the formation energies of more extended three-split and four-split vacancies. The relative formation energy of V_{Ga}^{ibc} [Fig. 3(h)] decreased by 0.42 eV in $1 \times 4 \times 3$ supercell, consistent with earlier findings by Frodason *et al.* [17]. The formation energies of V_{Ga}^{iab} and V_{Ga}^{iac} [Figs. S3(c) [23] and 3(i), respectively] also decreased by approximately 0.17 and 0.11, respectively, with $2 \times 4 \times 2$ supercells. In the case of four-split vacancies, a significant decrease in relative formation energies was observed for V_{Ga}^{iaba} and V_{Ga}^{iabc2} [Figs. S3(i) and S3(l) [23]] when using the $2 \times 4 \times 2$ supercell (reduced by 0.37 and 0.09 eV, respectively), as well as for V_{Ga}^{ibcb}, V_{Ga}^{iabc1}, and V_{Ga}^{iabc3} [Figs. S3(k), S3(h), and S3(m) [23]] when using the $1 \times 4 \times 3$ supercell (reduced by 0.53, 0.39, and 0.36 eV, respectively).

Among the identified vacancies, V_{Ga}^{ic} [Fig. 3(e)] exhibited the lowest formation energy, followed by V_{Ga}^{iabc2} and V_{Ga}^{iaba} [Figs. S3(i) and S3(l) [23]] with relative energy differences of only 0.06 and 0.11 eV, respectively. It should be noted that triple and four-split vacancies showed even lower formation energies compared to well-known two-split vacancies such as V_{Ga}^{ia} and V_{Ga}^{ib}, as well as point vacancies $V_{Ga(I)}$ and $V_{Ga(II)}$, highlighting the possibility of significantly longer stable split vacancy chains extending across multiple unit cells. Such vacancy chains, in turn, would require even larger supercells to accurately characterize.

Recent studies have explored the possibility that N-split defects play a role in the phase transition between the β and γ phases of Ga_2O_3 [42,43]. The γ phase, a metastable polymorph of Ga_2O_3 that exhibits the defect spinel structure, forms a disordered cation arrangement while sharing a similar anion lattice skeleton with the β phase [32,44]. Experimental investigations frequently observe the presence of γ-phase layers on the surfaces of β-Ga_2O_3 films grown under various conditions [45]. The γ-phase structures resemble the split interstitials observed in the A, B, and C hexagonal channels of β-Ga_2O_3; these interstitials can arise as part of the N-split vacancies. In recent theoretical work, Huang *et al.* proposed the formation of Ga defect complexes that involve relaxations of multiple Ga defects, probably two-split Ga vacancies, resulting in a local structure similar to the γ phase [42]. This structural analogy suggests the possibility that larger-scale formation of N-split Ga vacancies, extending beyond four-split throughout the bulk, could potentially induce a phase transition between the β and γ phase Ga_2O_3.

B. Diffusion networks and migration energy barriers

In the following sections, we first describe our approach and main findings for the interstitial and vacancy diffusion networks. These findings include components of the vacancy and interstitial diffusion tensors, effective activation energies, discussion of anisotropy, estimates of Ga cation self-diffusion coefficients, and comparison to available experiments. Finally, we subsequently break down the diffusion networks for interstitials and vacancies in detail to identify the dominant elementary hops and diffusion mechanisms.

1. Overall diffusivities and activation energies for interstitials and vacancies, $D_{Ga_i^{3+}}$ and $D_{V_{Ga}^{3-}}$

To construct 3D diffusion networks for interstitials Ga_i^{3+} and vacancies V_{Ga}^{3-}, we first identified all possible hops between defects with mid-points that lie within a distance of 4 Å. This analysis resulted in a significant number of unique hops, exceeding 200 for both interstitials and vacancies. To reduce computational burden, and given the likelihood that most hops could be decomposed into sequences of shorter substituent hops, we established a set of criteria to select a subset for first-principles NEB characterization, aiming to

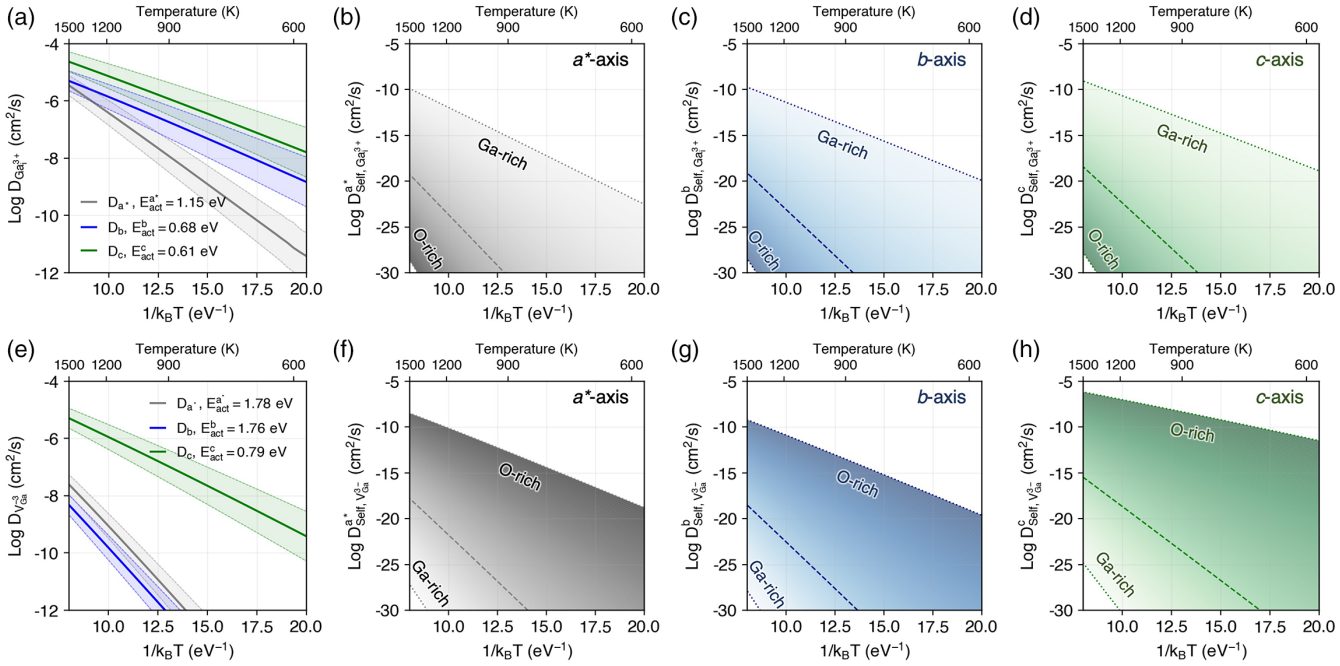

FIG. 4. Arrhenius plots of the diffusion coefficients (diagonal elements) of (a) Ga_i^{3+} and (e) V_{Ga}^{3-} along three crystallographic directions (a^*, b, c). The activation energies for each diffusion mechanism and direction are indicated. The shaded areas indicate the anticipated range of diffusivity variations due to an estimated uncertainty of 0.1 eV in migration energy barriers. Arrhenius plots illustrating the self-diffusion coefficients of Ga mediated by [(b)–(d)] Ga_i^{3+} and [(f)–(h)] V_{Ga}^{3-} along three different crystallographic directions (a^*, b, c). The dotted lines indicate the diffusivities in the Ga- or O-rich thermodynamic limit, while the dashed line denotes the intermediate state between Ga-rich and O-rich limits (halfway between Ga-rich and O-rich limits).

identify unique principal hops (PHs) that cannot be further decomposed.

For interstitial diffusion, we evaluated two key factors: (1) the number of ions undergoing large total displacements, and (2) the cumulative total displacement of all ions, between the initial and final configurations. These thresholds were first evaluated assuming simple linear ion movements connecting the starting and final configurations. Then, we performed initial NEB calculations using $1 \times 4 \times 2$ supercells for two subgroups of hops based on (1) hops for which no ions exceed a 1.5 Å threshold for total displacement, and (2) hops for which only one ion exceeded the displacement threshold while ensuring that the total summed ionic shifts remained below 10 Å, as illustrated in Fig. S7. During the NEB simulations, if new metastable structures were encountered along the migration energy landscape, we isolated them and performed structural optimization to understand how the corresponding hop could be decomposed into smaller hops, as summarized in Table S1. After all initial NEB calculations, hops that exhibited a single energy barrier and could not be further decomposed were identified as PHs of Ga_i^{3+}. Secondary NEB calculations were conducted for the identified PHs using larger supercells to mitigate finite-size effects. Supercells selected for these calculations were chosen from $1 \times 4 \times 3$, $2 \times 4 \times 2$, and $2 \times 4 \times 3$. The resulting NEB migration barriers for Ga_i^{3+} PHs are summarized in Table S2. Ultimately, we ended up with 32 unique hops for Ga interstitials.

For vacancy diffusion, we introduced an assumption that N-split vacancy diffusion always occurs via the formation of a (N-1)-split vacancy during the hop. This assumption is made to efficiently identify the PHs by avoiding concerted movements of ions, as those movements can always be decomposed into sequences of isolated atomic hops. For instance, a four-split vacancy will transition to one of the three-split vacancies first, rather than directly transforming into another four-split vacancy. After applying this assumption, we performed NEB calculations specifically for those hops where the total net ionic shift did not exceed 5 Å. The resulting NEB migration barriers for V_{Ga}^{3-} hops (31 in total) are summarized in Table S3 [23].

Once the diffusion pathways and their migration energy barriers were obtained from NEB calculations, the Onsager formalism [46] was utilized to obtain three-dimensional diffusivity tensors for Ga_i^{3+} and V_{Ga}^{3-}. Arrhenius plots for the a^*-, b-, and c-axis components are shown in Figs. 4(a) and 4(e) for interstitials and vacancies, respectively. The shaded region depicts the range of diffusivity variations associated with a ± 0.1 eV uncertainty in calculated migration barriers. For interstitial diffusion, the diffusion coefficients show the highest values along the c axis, followed by the b and a^*axes. For instance, at 600 K, the interstitial diffusion coefficients along the a^*, b, and c axes are 7.42×10^{-12}, 2.34×10^{-9}, and 2.43×10^{-8} cm^2/s, respectively. For vacancy diffusion, the diffusion coefficients are largest along the c axis, followed by much slower diffusion along both the a^* and b axes. At 600 K, the vacancy diffusion coefficients along the a^*, b, and c axes are 6.19×10^{-17}, 9.07×10^{-18}, and 6.61×10^{-10} cm^2/s, respectively. The anisotropy for vacancy diffusion is more pronounced than for interstitial diffusion,

with the c-axis diffusion coefficient more than 10^7 times larger than along the other axes.

The corresponding effective activation energies in Figs. 4(a) and 4(e) are 1.15, 0.68, and 0.61 eV for Ga_i^{3+} diffusion, and 1.76, 1.78, and 0.79 eV for V_{Ga}^{3-} diffusion along the a^*, b, and c axes, respectively. The anisotropy observed for both interstitials and vacancies can potentially influence a range of key material properties for β-Ga_2O_3. Anisotropic diffusion of vacancies or interstitials, as well as the implied anisotropic diffusion of Ga cations (self-diffusion) and/or extrinsic dopants, could have implications for devices and thermally activated degradation. For example, nonuniform diffusion with slow and fast directions could result in built-in fields that alter device performance. Many approaches to extrinsic doping such as ion implanation rely on diffusion, so the predicted anisotropy becomes particularly significant in situations where the diffusion of extrinsic cation dopants is mediated by vacancies or interstitials.

2. Ga self-diffusion and comparison to experiment

With the vacancy and interstitial diffusivities given above, it is possible to estimate the Ga cation self-diffusivity as well. Self-diffusion refers to the process in which host atoms migrate through the host lattice. Since self-diffusion is obtained as an average over all sites including mobile and immobile ions, the Ga self-diffusion coefficient is given by the product of the fractional concentration of Ga defects (here, Ga_i or V_{Ga}) and their respective defect diffusion coefficients [47,48]:

$$D_{\text{self,Defect}} = \frac{C_{\text{Defect}}}{C_{\text{Ga}}} D_{\text{Defect}}, \tag{2}$$

where Defect = Ga_i, V_{Ga}. This expression arises from consideration of jump balance. For example, the movement of Ga ions can occur via vacancy-mediated hopping: a Ga ion can jump to a neighboring Ga site if the neighboring site contains a vacancy. After the jump, the original site becomes vacant. Therefore the Ga ion hop is equivalent to a V_{Ga} hop to an adjacent occupied Ga site taking place in the opposite direction. In Eq. (2), C_{Defect} represents the concentration of migrating Ga defects, C_{Ga} denotes the total concentration of Ga sites in the bulk, and D_{Defect} is the diffusivity of the defect, obtained above. This equation also shows that, when defect concentrations are given by equilibrium, the activation energies for self-diffusion differ from those of isolated vacancies or interstitials. The difference is due to the term C_{Defect}, which introduces an additional contribution given by the defect formation energy, due to the thermally activated nature of the defect concentration.

From Eq. (2), were the concentrations of Ga interstitials and vacancies the same, then the slightly higher diffusivity of Ga_i^{3+} compared to V_{Ga}^{3-} [Figs. 4(a) and 4(e)] would imply that the self-diffusion of Ga to be mostly mediated by Ga interstitials. However, we find that the substantially higher vacancy concentration expected under common n-type doping or unintentionally doped (UID) conditions (as shown in Fig. S6 [23]) is sufficient to make Ga self-diffusion entirely dominated by vacancies. Figures 4(b)–4(d) and 4(f)–4(h) present Arrhenius plots for the self-diffusivities mediated by Ga interstitials (Ga_i^{3+}) and Ga vacancies (V_{Ga}^{3-}) across a wide spectrum of thermodynamic conditions, ranging from Ga-rich [low $P(O_2)$] to O-rich [high $P(O_2)$], respectively. These diffusivities are obtained under the assumption that the Fermi level is positioned at 3.0 eV [1.8 eV below the conduction band minimum (CBM)]. In an intermediate condition between Ga-rich and O-rich limits, depicted by dashed lines, self-diffusion coefficients for V_{Ga}^{3-} are predicted to be higher across all crystallographic axes, attributed to significant differences in equilibrium defect concentrations. For example, $D_{\text{self},V_{Ga}^{3-}} = 7.00 \times 10^{-19}$ cm^2/s but $D_{\text{self},Ga_i^{3+}} = 1.87 \times 10^{-22}$ cm^2/s along the c axis at 1200 K. In the O-rich limit, applicable to diffusion experiments at ambient pressures, the difference in Ga self-diffusion coefficients becomes more significant. Now, $D_{\text{self},V_{Ga}^{3-}} = 1.33 \times 10^{-7}$ cm^2/s and $D_{\text{self},Ga_i^{3+}} = 8.95 \times 10^{-34}$ cm^2/s along the c axis at 1200 K.

3. Comparison to experimental measurements of activation energies for defect migration

Experimental measurements of the activation energy for ionic diffusion or ionic conductivity are challenging, since multiple ionic transport processes can contribute to measured quantities. It is often difficult to know *a priori* which processes dominate. The simultaneous contribution of electrons to measured conductivities adds to the complexity of isolating ionic contributions alone. In semi-insulating or UID β-Ga_2O_3, where electronic contributions are largely suppressed, the diffusion of charged defects such as compensating V_O^{2+}, Ga_i^{3+}, and V_{Ga}^{3-} becomes the dominant contributor to charge transport. In such cases, the measured activation energy of carrier mobility or of conductivity is a reasonable estimate of the activation energy for charged defect diffusion.

Fleischer *et al.* reported activation energies for carrier mobility of 0.60 and 0.65 eV for UID crystal and ceramics, respectively [49]. Ghadbeigi *et al.* reported an activation energy of 0.86 eV for total conductivity in semi-insulating Mg-doped β-Ga_2O_3 under comparable contributions from electronic and ionic conduction [50]. As suggested by Kyrtsos *et al.*, migration barriers for V_O^{2+} are approximately 1 eV higher than for Ga_i^{3+} and V_{Ga}^{3-} [14], so these experimentally reported activation energies are likely attributed to the migration of charged Ga defects. Also, Ingebrigtsen *et al.* experimentally measured an activation energy of 1.2 eV using electrical conductivity recovery measurements [18] that they associated with gallium vacancy migration. However, these energies were obtained in proton implanted β-Ga_2O_3 in the context of the recovery of electronic charge carrier concentrations under subsequent annealing. More recently, Azarov *et al.* reported a migration barrier of 0.80 eV, determined by a dose-rate effect methodology, which assesses the impact of ion flux and temperature on lattice disorder and defect migration [51].

Overall, our calculated lowest migration barriers for Ga_i^{3+} and V_{Ga}^{3-} agree well with the findings of Fleischer *et al.*, Ghadbeigi *et al.*, and Azarov *et al.*, but not with the barrier of 1.2 eV reported by Ingebrigtsen *et al.* Although the reason for the discrepancy with Ingebrigtsen's result is not known, we suggest that it could be attributed to their measurement reflecting second-order kinetic processes in addition to vacancy migration during the thermal recovery process. Under

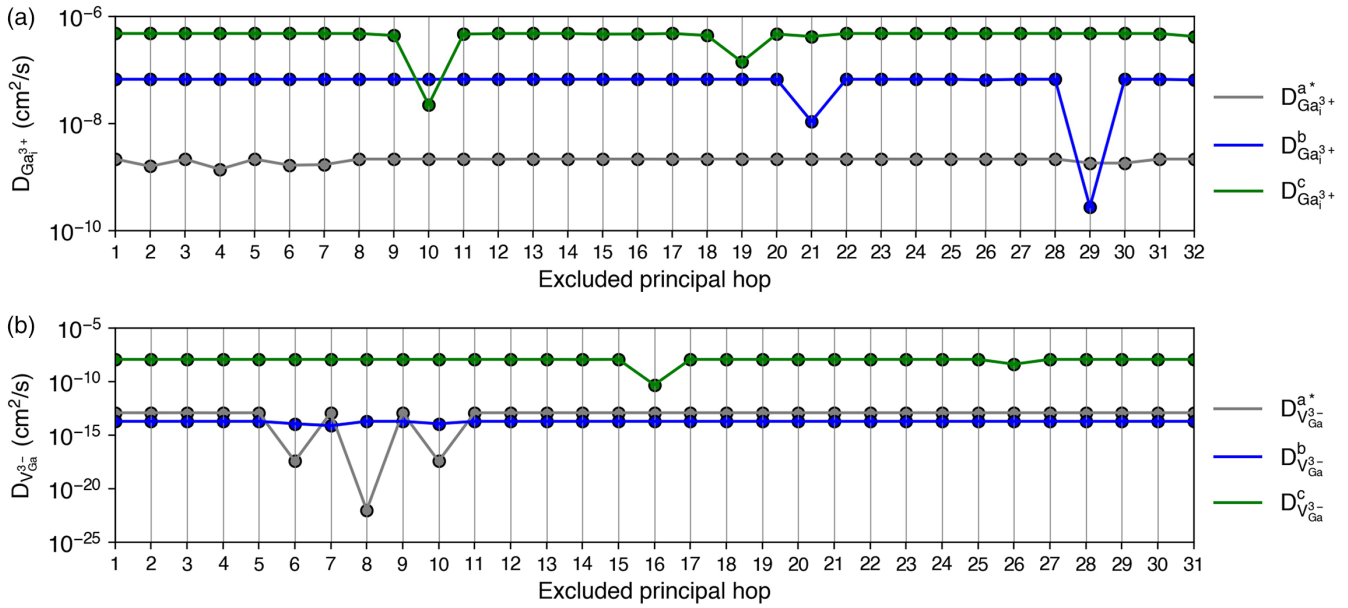

FIG. 5. By excluding each principal hop one-by-one in the diffusion calculations, the reduction of the diffusion coefficients of (c) Ga_i^{3+} and (d) V_{Ga}^{3-} at $T = 800$ K are indicated.

second-order kinetics, processes such as diffusion followed by subsequent defect trapping following reaction equations can introduce additional contributions to activation energies beyond the pure defect migration barriers.

4. Dominant migration pathways for interstitial diffusion

The diffusion coefficients and effective activation energies reported in Figs. 4(a) and 4(e) arise from the complete diffusion network, comprising all possible defect sites and all possible hops between them. These coefficients arise from multiple contributions. First, under equilibrium, the site probabilities ρ_i (see Appendix A) are described by Boltzmann statistics. The overall residence time for which a defect occupies a higher energy configuration is smaller than its residence time in lower energy configurations. Consequently, if diffusion along a particular crystallographic direction necessitates passing through a site with large energy (relative to other available sites), then the need to pass through this site introduces high-energy barriers. Second, even for transitions between two comparatively low-energy sites, the transition barrier through which the defect passes may be large, also slowing the diffusion. Under equilibrium (see Appendix A), transition rates obey detailed balance so that $\rho_i \lambda_{i\to j} = \rho_j \lambda_{j\to i}$ where $\lambda_{i\to j}$ is the transition rate from site i to site j and is proportional to $\exp(-\beta[E_{ij}^{ts} - E_i])$.

To identify the reasons underlying the differences in diffusivities along different crystallographic axes [Figs. 4(a) and 4(e)], it is necessary to first isolate the contribution of each PH and identify the sites and hops that are dominant contributors to diffusion in each crystallographic direction. For this, we constructed reduced diffusion networks by excluding one PH at a time from the full set of principal hops for Ga_i^{3+} diffusion. As shown in Fig. 5, by comparing the resulting diffusivities with those obtained from the full set described in the previous section, we were able to assess the contribution of each PH to the total diffusivity. For example, when PH 10 or PH 19 is removed from the diffusion network of Ga_i^{3+} [Fig. 5(a)], a substantial decrease in diffusivity along the c axis is observed, indicating the critical role of these two hops in facilitating Ga_i^{3+} diffusion along the c axis. After identifying dominant contributors, we constructed additional reduced diffusion networks that included only these core PHs and compared its diffusivity with that of the full set, allowing us to isolate the set of active diffusion pathways formed by combinations of core PHs. Through this analysis, we determined the dominant diffusion pathways for Ga_i^{3+} diffusion along each crystallographic direction. These pathways and the corresponding energy landscapes are illustrated in Fig. 6.

For Ga_i^{3+} diffusion along the a^* axis (the slowest axis), we aimed to identify the main energy barriers. We identified three major hopping pathways which are shown in Figs. 6(a)–6(c). The pathways shown in Figs. 6(a) and 6(b) are associated with ac-plane diffusion, following the Ga_{iac}- Ga_{iaca}-Ga_{iac} and Ga_{iab}- Ga_{iaba}-Ga_{iab} routes shown in Fig. 6(e). The associated energy landscapes are shown in Figs. 6(h) and 6(i). The landscapes show that diffusion along a^* requires passing through the high energy Ga_{ia} site, which is 1.01 eV higher in energy than the lowest energy Ga_{iac} site. For both of these paths, we observe similar rate-limiting steps, defined here as the highest energy barrier for an isolated hop within the path, in which a favorable split interstitial (Ga_{iac} or Ga_{iad}) diffuses across the hexagonal channel along the b axis to a high-energy Ga_{ia} configuration with migration energies of approximately 1.16 and 0.92 eV. In the alternative a^* pathway of Figs. 6(c) and 6(j), a slightly more complex route, the quadruple split interstitial Ga_{iadcc} is employed to bypass the high-energy Ga_{ia} state. Unfortunately, this route suffers from a large transition barrier however, 0.72 eV between Ga_{iadcc} and Ga_{icac}. By comparing the diffusivity of reduced diffusion networks that include each

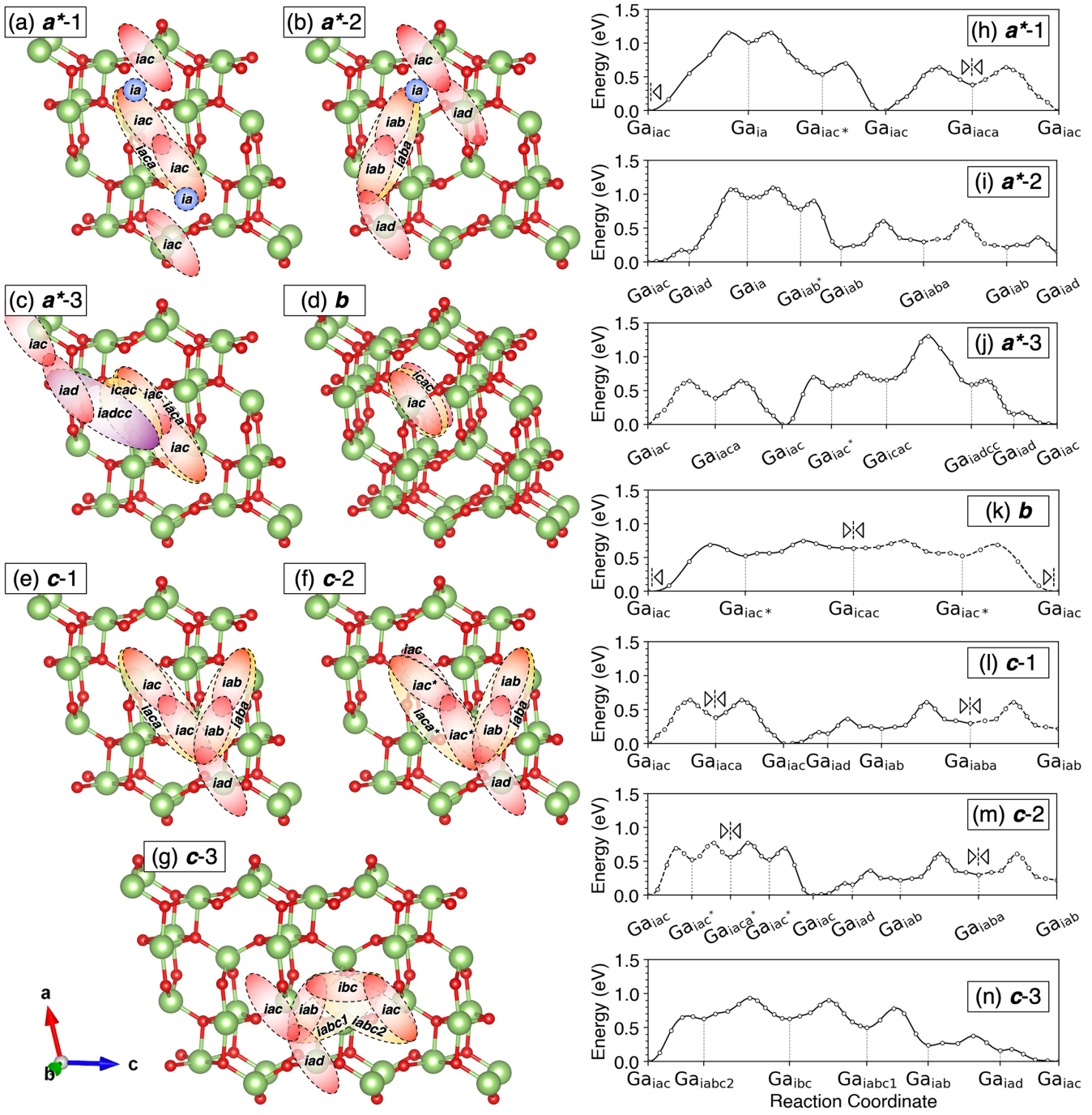

FIG. 6. Schematic illustrations of dominant diffusion pathways of Ga_i^{3+} along [(a)–(c)] a^*-axis, (d) b-axis, and [(e)–(g)] c-axis crystal orientations, respectively. [(h)–(n)] Corresponding energy landscapes along the energy minimum pathways. Overlapping principal interstitial hops within the diffusion pathways are represented by dashed lines in the energy profiles. Mirror symbols at selected points indicate that only half of the reaction is shown, and that the full reaction is completed by mirroring the path at the point indicated.

set of selected PHs in Figs. 6(a)–6(c), we obtained a^*-axis diffusivities of 38%, 44%, and 16% from the total a^*-axis diffusivity, respectively. When including all hops in (a)–(c), we achieve 98% of the diffusivity, indicating that these three paths make up the main diffusion pathways along the a^* axis.

Regarding b axis diffusion, the direction with intermediate diffusivity, we identified one major diffusion pathway [Figs. 6(d) and 6(k)]. In this pathway, the Ga_{iac} interstitial moves across the hexagonal channel along the b axis and forms a symmetric three-split interstitial, Ga_{icac}. Unlike the a^* direction, there is no need to pass through high energy sites like Ga_{ia}, the interstitial remains as a split throughout the entire path, and the energy profile in Fig. 6(k) is smooth compared to the paths in Figs. 6(h), 6(i), and 6(j). The highest site energy of 0.64 eV is associated with Ga_{icac}. The rate-limiting step occurs during the Ga_{iac}-Ga_{iac^*} process with transition barrier of 0.69 eV, where the split interstitial deviates from the ac-plane along with the other ic Ga split interstitial and

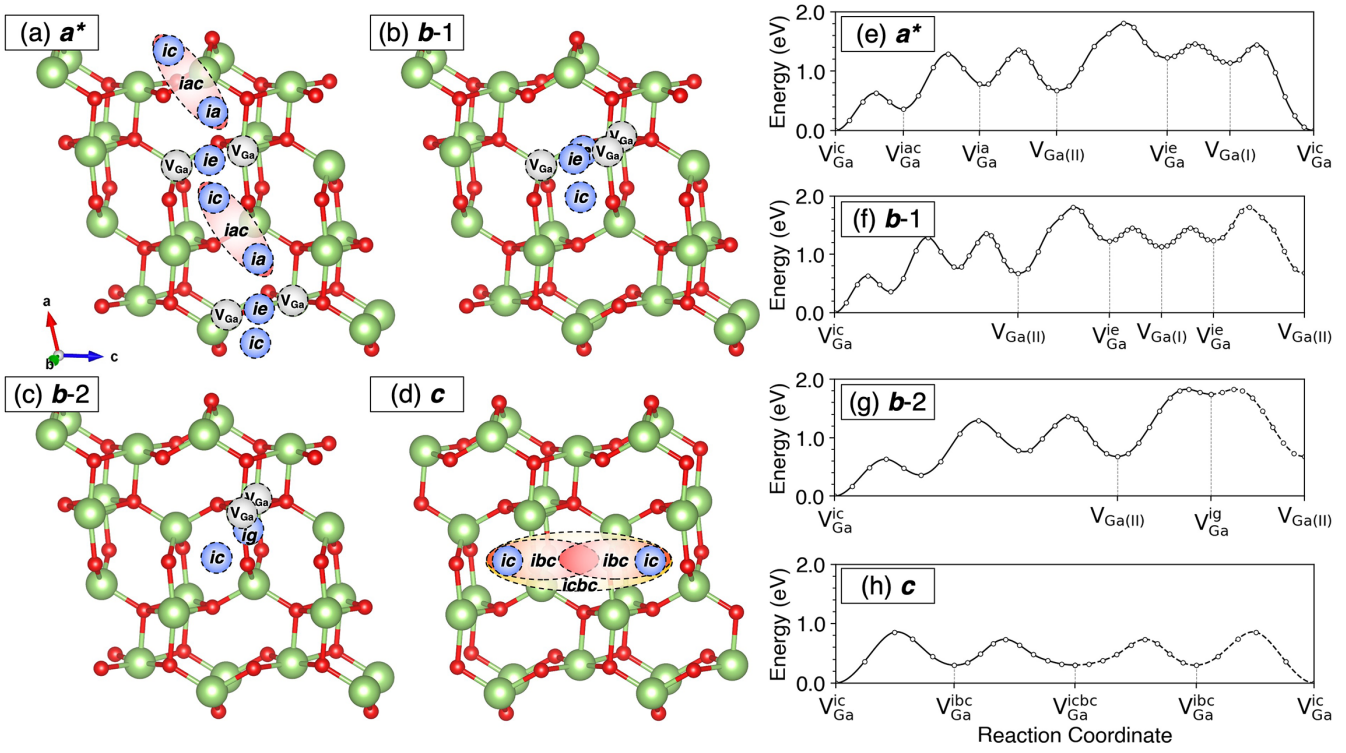

FIG. 7. Schematic illustrations of dominant diffusion pathways of V_{Ga}^{3-} along (a) a^*-axis, [(b) and (c)] b-axis, and (d) c-axis crystal orientations, respectively. [(e)–(h)] Corresponding energy landscapes along the energy minimum pathways.

two Ga vacancies, resulting in the loss of b-axis symmetry. This hopping pathway accounts for over 97% of the diffusivity along the b axis.

For c-axis diffusion (the fastest direction), we identified three contributing diffusion pathways. The pathways are illustrated in Figs. 6(e)–6(g), and the potential energy surfaces are shown in Figs. 6(l)–6(n). Similar to diffusion along the a^* axis, fast in-plane diffusion pathways are observed following the Ga_{iab}-Ga_{iaba}-Ga_{iab} and Ga_{iac}-Ga_{iaca}-Ga_{iac} routes, as shown in Figs. 6(e) and 6(l). In the pathway of Figs. 6(f) and 6(m), the Ga_{iac}-Ga_{iac^*} process is involved, resulting in another side path, Ga_{iac^*}-Ga_{iaca^*}-Ga_{iac^*}, with moderate migration barriers. In the pathway of Figs. 6(g) and 6(n), the Ga_{ibc} site is utilized to connect the three-split interstitials of Ga_{iabc1} and Ga_{iabc2}. By comparing the diffusivity of reduced diffusion networks these three paths, we obtained diffusivities of 84%, 26%, and 3% of the c-axis total diffusivity, respectively. Considering all hops in Figs. 6(e)–6(g), we achieve 99% of the diffusivity. Since all c-axis diffusion pathways occur predominantly within the ac plane, the migration barriers are smaller compared to the other two directions, resulting in higher diffusivities along c compared to a^* and b.

Overall, we attribute the higher diffusivity along c compared to b to the availability of multiple paths, some of which show slightly lower barriers than the single path available for b-axis diffusion. Compared to the b direction, the three c-axis pathways involve sites of similar site energies. For path c-1, we have Ga_{iaca} (0.39 eV) and Ga_{iaba} (0.30 eV). For path c-2, we have Ga_{iac^*} (0.53 eV) and Ga_{iaca^*} (0.57 eV). And for path c-3, we have Ga_{iabc2} (0.63 eV), Ga_{ibc} (0.63 eV), and Ga_{iabc1} (0.50 eV). The associated rate limiting barriers for each path are 0.64, 0.69, and 0.66 eV, respectively. The overall pathway barriers for each path, defined as the difference between the lowest and highest energy overall along the full path, are 0.64, 0.77, and 0.94 eV, respectively.

5. Dominant migration pathways for vacancy diffusion

We also explored the dominant pathways for V_{Ga}^{3-} diffusion along each crystallographic direction. The dominant pathways and their corresponding energy landscapes are illustrated in Fig. 7. Along the a^* axis (a very slow direction), we identified one predominant pathway, shown in Figs. 7(a) and 7(e). The landscape indicates that diffusion along a^* necessitates passing through several high-energy states, including $V_{Ga(I)}$ and V_{Ga}^{ie}, with site energies that are 1.14 and 1.22 eV above the lowest energy V_{Ga}^{ic} state, respectively. The path starts with elementary hops between the lowest-energy two-split V_{Ga}^{ic} and the three-split V_{Ga}^{iac}, which occurs via a Ga(II) ion moving into the *ia* interstitial site. In the adjacent unit cell, the *ic* split interstitial (present as part of V_{Ga}^{iac}) moves to the Ga(I) site to form V_{Ga}^{ia}. Next, the *ia* split interstitial (present as part of V_{Ga}^{ia}) moves to the Ga(I) site, leaving $V_{Ga(II)}$. Then, Ga(I) moves into the *ie* split intersititial site, forming two-split V_{Ga}^{ie}. Finally, the *ie* split interstitial (present as part of V_{Ga}^{ie}) moves to Ga(II). The rate-limiting step, with a migration barrier of 1.13 eV, occurs during the $V_{Ga(II)}$-V_{Ga}^{ie}-$V_{Ga(I)}$ process, involving ionic movements along the b axis. This hopping pathway accounts for over 99% of the diffusivity along the a^* axis.

For b-axis diffusion (the slowest direction), we identified two major pathways. These are illustrated in Figs. 7(b) and 7(c) and their energy landscapes are given in Figs. 7(f) and 7(g). Similar to the a^*, the diffusion path b-1 necessitates passing through high energy states of $V_{Ga(I)}$ and V_{Ga}^{ie}. This path

follows the $V_{Ga(II)}$-V_{Ga}^{ie}-$V_{Ga(I)}$ process similar to Figs. 7(a) and 7(e) and shows a rate-limiting barrier of 1.13 eV. The second path in Figs. 7(c) and 7(g) proceeds directly along the *b* axis by passing through V_{Ga}^{ig}, with high site energy of 1.74 eV. It follows the $V_{Ga(II)}$-V_{Ga}^{ig}-$V_{Ga(II)}$ route; the rate-limiting barrier of 1.15 eV occurs when passing through V_{Ga}^{ig}. By comparing the diffusivity of reduced diffusion networks, we obtain diffusivities of 60% and 40% of the *b*-axis diffusivity, respectively. Considering all hops in Figs. 7(b) and 7(c), we achieve 99% of the total diffusivity.

In the case of *c*-axis diffusion, substantially faster than the other two directions, one major pathway is identified, depicted in Figs. 7(d) and 7(h). Unlike diffusion along the a^* and *b* axes, the vacancy moves directly along the *c* axis by passing through low-energy states of V_{Ga}^{ibc} and V_{Ga}^{icbc}, with site energies for both of only 0.30 eV, thereby avoiding high-energy states. This pathway involves splitting of the lowest-energy two-split V_{Ga}^{ic} into the three-split V_{Ga}^{ibc}. Instead of the V_{Ga}^{ic}-V_{Ga}^{ibc}-V_{Ga}^{ic} route proposed by Frodason *et al.* [17], the presence of the additionally extended four-split V_{Ga}^{icbc} allows bypassing the V_{Ga}^{ic}-V_{Ga}^{ibc} energy barrier, resulting in a different V_{Ga}^{ic}-V_{Ga}^{ibc}-V_{Ga}^{icbc}-V_{Ga}^{ibc}-V_{Ga}^{ic} route. The rate-limiting step occurs along V_{Ga}^{ic}-V_{Ga}^{ibc}, with a barrier of 0.86 eV. This hopping pathway accounts for over 99% of the diffusivity along the *c* axis. Here, the identification of the four-split V_{Ga}^{icbc} creating the lowest energy pathway highlights the potential for exploiting further extended *N*-split vacancies ($N \geqslant 4$) to access new low-energy diffusion paths and suggests that further exploration of more extended *N*-split defects on larger scales could be fruitful.

6. Comparison to results of Frodason et al.

Overall, our predictions for the dominant diffusion pathways are largely in agreement with and show only minor differences with those proposed by Frodason *et al.* [17]

Regarding the diffusion of Ga_i^{3+}, we predict the fastest diffusion along *c*, followed by *b*, and then a^*. In contrast, Frodason *et al.* suggest the order to be a^*, *c*, and *b* axes. This discrepancy can be attributed to the reduced energy barriers for both Ga_{iaba} and Ga_{iaca} transition states obtained here, which are critical for diffusion along the *c* axis. This reduction was observed after employing larger $2 \times 4 \times 2$ supercells in our simulations. For *c*-axis diffusion, we predict the fastest pathway as Ga_{iac}-Ga_{iad}-Ga_{iab}, while Frodason *et al.* suggest the Ga_{iac}-Ga_{iab} route. Both studies agree on the diffusion route along the *b* axis. Lastly, for a^*-axis diffusion, we predict the fastest route along in the Ga_{iac}-Ga_{iac^*}-Ga_{ia}-Ga_{iac} route, while Frodason *et al.* suggest the Ga_{iac}-Ga_{iac^*}-Ga_{if}-Ga_{ia}-Ga_{iac} route.

Regarding the V_{Ga}^{3-} diffusion pathways, both studies agree on the order of fast diffusion directions as *c*, a^*, and *b* axes. Both studies also predict the same routes along the a^* and *b* axes. However, we introduce a slightly modified route for *c*-axis diffusion by incorporating the three-split V_{Ga}^{icbc} structure. The three-split defect V_{Ga}^{icbc} creates a locally metastable arrangement, allowing the avoidance of alternative configurations linked to high energy barriers. As a result, without the inclusion of V_{Ga}^{icbc}, vacancy diffusion coefficient along the *c* axis at 600 K is found to be 1.68×10^{-10} cm^2/s, whereas it rises to 6.61×10^{-10} cm^2/s after including V_{Ga}^{icbc}, showing that including the extended defect enhances the diffusivity by approximately half an order of magnitude.

We also note that the results of Frodason *et al.* [17] were obtained by HSE calculations rather than PBE as used here. However, we believe that the minor differences between the two studies arise for reasons unrelated to the choice of functional (see Fig. S8 [23]) and are mostly related to treatment of finite size effects and inclusion of additional extended defects. Despite minor differences, the overall agreement between two independent studies gives credence to the findings and highlights the importance of *N*-split defects in understanding the diffusion mechanisms of β-Ga_2O_3.

IV. CONCLUSION

We used first-principles calculations to explore various Ga native defect configurations in β-Ga_2O_3, including *N*-split defects, and analyzed operative vacancy and interstitial diffusion networks. By employing the Onsager approach, we formulate the master diffusion equations for Ga interstitials and Ga vacancies by constructing a 3D diffusion network from a comprehensive set of 32 unique interstitial and interstitialcy hops between 20 different configurations of Ga interstitials and 31 unique vacancy hops between 19 different configurations of Ga vacancies. The solution of these equations yields the three-dimensional diffusivity tensors. Both Ga interstitials and vacancies demonstrated the highest diffusivity along the *c* axis with calculated diffusivities of 8.89×10^{-6} and 1.45×10^{-6} cm^2/s at $T = 1200$ K, corresponding to the lowest effective activation energies of 0.61 and 0.79 eV, respectively. However, Ga self-diffusion is ultimately mediated by vacancies, because of the substantially higher concentration of Ga vacancies than Ga interstitials; For instance, we estimate self-diffusion coefficients of 1.33×10^{-7} and 8.95×10^{-34} cm^2/s for processes mediated by Ga_i^{3+} and V_{Ga}^{3-} at $T = 1200$ K under the O-rich condition, respectively. We also identified the dominant diffusion mechanism in each crystallographic direction. We hope these findings improve the understanding of intrinsic defect diffusion in β-Ga_2O_3, and help in understanding degradation and other mass transport related phenomena in high-performance power devices.

The data that support the findings of this study are available on GitHub [52].

ACKNOWLEDGMENTS

The authors acknowledge the funding provided by the Air Force Office of Scientific Research under Award No. FA9550-21-0078. This work used PSC Bridges-2 at the Pittsburgh Supercomputing Center through allocation MAT220011 from the Advanced Cyberinfrastructure Coordination Ecosystem: Services & Support (ACCESS) program, which is supported by National Science Foundation Grants No. 2138259, No. 2138286, No. 2138307, No. 2137603, and No. 2138296.

APPENDIX A: DIRECT ONSAGER APPROACH: DIFFUSIVITY CALCULATION

The Onsager approach for obtaining diffusivity tensors is based on several key assumptions. First, it is assumed that

defects undergo harmonic motion within the crystal lattice, allowing for simplification of the master diffusion equations to describe the time evolution of the system. Second, it is assumed that the equilibrium site probabilities ρ_i follow a Boltzmann relationship amongst thermally occupied energy states, given by

$$\rho_i = \frac{1}{Z}\rho_i^0 \exp(-\beta E_i), \tag{A1}$$

where $\rho_i^0 = \exp(\frac{S_i}{k_B})$ represents the entropic prefactor for the static state, estimated here to be uniformly 1 for all configurations. Here, Z is the partition function, which is defined by the sum of the Boltzmann factors over all available states as $Z = \sum_i \rho_i^0 \exp(-\beta E_i)$. Third, from transition state theory, it is assumed that the transition rates $\lambda_{i\to j}$ under dilute conditions follow

$$\lambda_{i\to j} = \frac{\lambda_{ij}^0}{\rho_i^0} \exp\big(-\beta\big[E_{ij}^{ts} - E_i\big]\big), \tag{A2}$$

where $\lambda_{ij}^0 = \exp(\frac{S_{ij}^{ts}}{k_B})$ represents the entropic prefactor for the transition state, i.e. the attempt frequency for the particular jump. In our work, we approximate this prefactor using a typical phonon frequency of 10^{13} Hz [14,17].

With site energies and transition barriers enumerated and obtained from first-principles, the Onsager software package [22] is used to construct the master diffusion equations. The steady-state solution of these equations results in the diffusion tensor D, which can be expressed as

$$D = \frac{1}{2}\sum_{ij} \delta x_{i\to j} \otimes \delta x_{i\to j} \lambda_{i\to j} \rho_i + \sum_i b_i \otimes \gamma_i. \tag{A3}$$

Here, $\delta x_{i\to j} = x_j - x_i$ represents the displacement of the diffusing defect from state i to state j, ρ_i is the equilibrium site probability for site i, b_i is the scaled velocity vector representing the bias of jumps at site i, and γ_i is the bias-correction vector obtained by solving $\sum_j \omega_{ij}\gamma_j = b_i$, which accounts for correlations arising from unbalanced forward and backward jumps due to the varying local atomic environment.

APPENDIX B: DEFECT FORMATION ENERGY CALCULATION

To obtain the defect formation energies and charge transition levels for Ga defects, we followed the standard supercell approach [53–55]. The formation energy $E_f[X^q]$ of a defect X in charge state q was obtained by determining the energy difference between the supercell containing the defect X and the pristine bulk β-Ga_2O_3 supercell according to

$$E_f[X^q] = E_{\text{tot}}[X^q] - E_{\text{tot}}[\text{Bulk}] - n\mu_{\text{Ga}} + qE_{\text{Fermi}} + E_{\text{corr}}. \tag{B1}$$

Here, $E_{\text{tot}}[X^q]$ and $E_{\text{tot}}[\text{Bulk}]$ represent the total energy of the supercell containing defect X in charge state q and the total energy of the host pristine supercell, respectively. The term μ_{Ga} represents the Ga chemical potential, and $n = 1$ ($n = -1$) when a Ga species is added to (removed from) the supercell to create the defect. The charging of defects involves the exchange of electrons with the electron chemical potential (semiconductor Fermi level, E_{Fermi}), typically referenced to the valence-band maximum.

Two limits were considered as the upper and lower bounds for the Ga chemical potential. In the upper limit (Ga-rich), μ_{Ga} is given by the energy per Ga atom in the pure elemental Ga phase (μ_{Ga}^0). In the lower limit (O-rich), μ_{O} is given by half of the energy of an O_2 molecule (μ_{O}^0) under 1 atm and 1000 K conditions. In this latter case, μ_{Ga} is shifted from μ_{Ga}^0 following the thermodynamic stability condition $\mu_{\text{Ga}} = \mu_{\text{Ga}}^0 + \frac{1}{2}\Delta H_f(\beta\text{-}Ga_2O_3)$, where $\Delta H_f(\beta\text{-}Ga_2O_3)$ is the calculated formation energy of β-Ga_2O_3 (10.78 eV per f.u.).

To compensate for the finite-size effects caused by electrostatic interactions between charged defects in neighboring supercells, we incorporated the energy correction term E_{corr}. We adopted the methodology proposed by Lany and Zunger [54] to estimate the energy corrections for potential alignment $\Delta E_{\text{pa}}(D, q)$ and image charge ΔE_{i}, expressed by

$$\Delta E_{\text{pa}}(D, q) = q\,\Delta V_{\text{pa}}, \tag{B2}$$

$$\Delta E_{\text{i}} = \frac{q^2\alpha_M}{2\epsilon\omega^{-1/3}}. \tag{B3}$$

Here, ΔE_{pa} represents the potential alignment between the defect and the host supercell, α denotes the Madelung constant specific to the supercell geometry, ϵ corresponds to the static dielectric constant, and ω represents the volume of the supercell.

[1] J. B. Varley, B. Shen, and M. Higashiwaki, Wide bandgap semiconductor materials and devices, J. Appl. Phys. **131**, 230401 (2022).

[2] S. Fujita, Wide-bandgap semiconductor materials: For their full bloom, Jpn. J. Appl. Phys. **54**, 030101 (2015).

[3] M. D. McCluskey, Point defects in Ga_2O_3, J. Appl. Phys. **127**, 101101 (2020).

[4] C. Lee, N. D. Rock, A. Islam, M. A. Scarpulla, and E. Ertekin, Electron-phonon effects and temperature-dependence of the electronic structure of monoclinic β-Ga_2O_3, APL Mater. **11**, 011106 (2023).

[5] M. Higashiwaki, A. Kuramata, H. Murakami, and Y. Kumagai, State-of-the-art technologies of gallium oxide power devices, J. Phys. D: Appl. Phys. **50**, 333002 (2017).

[6] M. Higashiwaki, K. Sasaki, H. Murakami, Y. Kumagai, A. Koukitu, A. Kuramata, T. Masui, and S. Yamakoshi, Recent progress in Ga_2O_3 power devices, Semicond. Sci. Technol. **31**, 034001 (2016).

[7] M. Kim, J.-H. Seo, U. Singisetti, and Z. Ma, Recent advances in free-standing single crystalline wide band-gap semiconductors and their applications: GaN, SiC, ZnO, β-Ga_2O_3, and diamond, J. Mater. Chem. C **5**, 8338 (2017).

[8] A. Azarov, V. Venkatachalapathy, L. Vines, E. Monakhov, I.-H. Lee, and A. Kuznetsov, Activation energy of silicon diffusion in gallium oxide: Roles of the mediating defects charge states and phase modification, Appl. Phys. Lett. **119**, 182103 (2021).

[9] A. Mauze, Y. Zhang, T. Itoh, T. E. Mates, H. Peelaers, C. G. Van de Walle, and J. S. Speck, Mg doping and diffusion in (010) β-Ga_2O_3 films grown by plasma-assisted molecular beam epitaxy, J. Appl. Phys. **130**, 235301 (2021).

[10] H. Peelaers, J. L. Lyons, J. B. Varley, and C. G. Van de Walle, Deep acceptors and their diffusion in Ga_2O_3, APL Mater. **7**, 022519 (2019).

[11] Y. K. Frodason, P. P. Krzyzaniak, L. Vines, J. B. Varley, C. G. Van de Walle, and K. M. H. Johansen, Diffusion of Sn donors in β-Ga_2O_3, APL Mater. **11**, 041121 (2023).

[12] P. M. Fahey, P. B. Griffin, and J. D. Plummer, Point defects and dopant diffusion in silicon, Rev. Mod. Phys. **61**, 289 (1989).

[13] J. M. Johnson, Z. Chen, J. B. Varley, C. M. Jackson, E. Farzana, Z. Zhang, A. R. Arehart, H.-L. Huang, A. Genc, S. A. Ringel, C. G. Van de Walle, D. A. Muller, and J. Hwang, Unusual formation of point-defect complexes in the ultrawide-band-gap semiconductor β-Ga_2O_3, Phys. Rev. X **9**, 041027 (2019).

[14] A. Kyrtsos, M. Matsubara, and E. Bellotti, Migration mechanisms and diffusion barriers of vacancies in Ga_2O_3, Phys. Rev. B **95**, 245202 (2017).

[15] M. A. Blanco, M. B. Sahariah, H. Jiang, A. Costales, and R. Pandey, Energetics and migration of point defects in Ga_2O_3, Phys. Rev. B **72**, 184103 (2005).

[16] J. B. Varley, H. Peelaers, A. Janotti, and C. G. V. de Walle, Hydrogenated cation vacancies in semiconducting oxides, J. Phys.: Condens. Matter **23**, 334212 (2011).

[17] Y. K. Frodason, J. B. Varley, K. M. H. Johansen, L. Vines, and C. G. Van de Walle, Migration of Ga vacancies and interstitials in β-Ga_2O_3, Phys. Rev. B **107**, 024109 (2023).

[18] M. E. Ingebrigtsen, A. Y. Kuznetsov, B. G. Svensson, G. Alfieri, A. Mihaila, U. Badstübner, A. Perron, L. Vines, and J. B. Varley, Impact of proton irradiation on conductivity and deep level defects in β-Ga_2O_3, APL Mater. **7**, 022510 (2018).

[19] C. Zimmermann, V. Rønning, Y. Kalmann Frodason, V. Bobal, L. Vines, and J. B. Varley, Primary intrinsic defects and their charge transition levels in β–Ga_2O_3, Phys. Rev. Mater. **4**, 074605 (2020).

[20] D. R. Trinkle, Diffusivity and derivatives for interstitial solutes: activation energy, volume, and elastodiffusion tensors, Philos. Mag. **96**, 2714 (2016).

[21] D. R. Trinkle, Automatic numerical evaluation of vacancy-mediated transport for arbitrary crystals: Onsager coefficients in the dilute limit using a Green function approach, Philos. Mag. **97**, 2514 (2017).

[22] D. Trinkle and A. Jain, Onsager v1.3.3, doi:10.5281/zenodo.3355730.

[23] See Supplemental Material at http://link.aps.org/supplemental/10.1103/PhysRevMaterials.8.054603 for additional illustrations, formation energies, migration barriers, and detailed diffusion mechanisms of Ga defects in β-Ga_2O_3.

[24] P. Hohenberg and W. Kohn, Inhomogeneous electron gas, Phys. Rev. **136**, B864 (1964).

[25] W. Kohn and L. J. Sham, Self-consistent equations including exchange and correlation effects, Phys. Rev. **140**, A1133 (1965).

[26] P. E. Blöchl, Projector augmented-wave method, Phys. Rev. B **50**, 17953 (1994).

[27] G. Kresse and D. Joubert, From ultrasoft pseudopotentials to the projector augmented-wave method, Phys. Rev. B **59**, 1758 (1999).

[28] G. Kresse and J. Furthmüller, Efficient iterative schemes for *ab initio* total-energy calculations using a plane-wave basis set, Phys. Rev. B **54**, 11169 (1996).

[29] G. Kresse and J. Furthmüller, Efficiency of ab-initio total energy calculations for metals and semiconductors using a plane-wave basis set, Comput. Mater. Sci. **6**, 15 (1996).

[30] J. P. Perdew, K. Burke, and M. Ernzerhof, Generalized gradient approximation made simple, Phys. Rev. Lett. **77**, 3865 (1996).

[31] J. P. Perdew and Y. Wang, Accurate and simple analytic representation of the electron-gas correlation energy, Phys. Rev. B **45**, 13244 (1992).

[32] S. Yoshioka, H. Hayashi, A. Kuwabara, F. Oba, K. Matsunaga, and I. Tanaka, Structures and energetics of Ga_2O_3 polymorphs, J. Phys.: Condens. Matter **19**, 346211 (2007).

[33] T. Zacherle, P. C. Schmidt, and M. Martin, *Ab initio* calculations on the defect structure of β-Ga_2O_3, Phys. Rev. B **87**, 235206 (2013).

[34] S. Geller, Crystal Structure of β-Ga_2O_3, J. Chem. Phys. **33**, 676 (1960).

[35] J. Åhman, G. Svensson, and J. Albertsson, A reinvestigation of β-gallium oxide, Acta Crystallogr. Sect. C **52**, 1336 (1996).

[36] A. Goyal, P. Gorai, H. Peng, S. Lany, and V. Stevanović, A computational framework for automation of point defect calculations, Comput. Mater. Sci. **130**, 1 (2017).

[37] H. J. Monkhorst and J. D. Pack, Special points for Brillouin-zone integrations, Phys. Rev. B **13**, 5188 (1976).

[38] G. Henkelman, B. P. Uberuaga, and H. Jónsson, A climbing image nudged elastic band method for finding saddle points and minimum energy paths, J. Chem. Phys. **113**, 9901 (2000).

[39] J. Sun, A. Ruzsinszky, and J. P. Perdew, Strongly constrained and appropriately normed semilocal density functional, Phys. Rev. Lett. **115**, 036402 (2015).

[40] J. Heyd, G. E. Scuseria, and M. Ernzerhof, Hybrid functionals based on a screened Coulomb potential, J. Chem. Phys. **118**, 8207 (2003).

[41] J. Heyd, G. E. Scuseria, and M. Ernzerhof, Erratum: "Hybrid functionals based on a screened Coulomb potential" [J. Chem. Phys. 118, 8207 (2003)], J. Chem. Phys. **124**, 219906 (2006).

[42] H.-L. Huang, J. M. Johnson, C. Chae, A. Senckowski, M. H. Wong, and J. Hwang, Atomic scale mechanism of β to γ phase transformation in gallium oxide, Appl. Phys. Lett. **122**, 251602 (2023).

[43] H.-L. Huang, C. Chae, J. M. Johnson, A. Senckowski, S. Sharma, U. Singisetti, M. H. Wong, and J. Hwang, Atomic scale defect formation and phase transformation in Si implanted β-Ga2O3, APL Mater. **11**, 061113 (2023).

[44] C. Wouters, M. Nofal, P. Mazzolini, J. Zhang, T. Remmele, A. Kwasniewski, O. Bierwagen, and M. Albrecht, Unraveling the atomic mechanism of the disorder-order phase transition from γ-Ga_2O_3 to β-Ga_2O_3, APL Mater. **12**, 011110 (2024).

[45] C. S. Chang, N. Tanen, V. Protasenko, T. J. Asel, S. Mou, H. G. Xing, D. Jena, and D. A. Muller, γ-phase inclusions

as common structural defects in alloyed β-$(Al_xGa_{1-x})_2O_3$ and doped β-Ga_2O_3 films, APL Mater. **9**, 051119 (2021).

[46] L. Onsager, Crystal statistics. I. A two-dimensional model with an order-disorder transition, Phys. Rev. **65**, 117 (1944).

[47] A. Kabir, H. Zhang, and V. Esposito, 5 - mass diffusion phenomena in cerium oxide, in *Cerium Oxide (*CeO_2*): Synthesis, Properties and Applications*, Metal Oxides, edited by S. Scirè and L. Palmisano (Elsevier, Amsterdam, Netherlands, 2020), pp. 169–210.

[48] S. Kasap and P. Capper, *Springer Handbook of Electronic and Photonic Materials* (Springer, Cham, Switzerland, 2017).

[49] M. Fleischer and H. Meixner, Electron mobility in single- and polycrystalline Ga_2O_3, J. Appl. Phys. **74**, 300 (1993).

[50] L. Ghadbeigi, R. Sun, J. Jesenovec, A. Bhattacharyya, J. McCloy, S. Krishnamoorthy, M. A. Scarpulla, and B. Sensale-Rodriguez, Electronic and ionic conductivity in β-Ga_2O_3 single crystals, J. Appl. Phys. **131**, 085102 (2022).

[51] A. Azarov, V. Venkatachalapathy, E. V. Monakhov, and A. Y. Kuznetsov, Dominating migration barrier for intrinsic defects in gallium oxide: Dose-rate effect measurements, Appl. Phys. Lett. **118**, 232101 (2021).

[52] C. Lee and E. Ertekin, https://github.com/ertekin-research-group/2024-Ga2O3-Ga-Diffusion.

[53] C. Freysoldt, B. Grabowski, T. Hickel, J. Neugebauer, G. Kresse, A. Janotti, and C. G. Van de Walle, First-principles calculations for point defects in solids, Rev. Mod. Phys. **86**, 253 (2014).

[54] S. Lany and A. Zunger, Accurate prediction of defect properties in density functional supercell calculations, Modell. Simul. Mater. Sci. Eng. **17**, 084002 (2009).

[55] J. M. Adamczyk, L. C. Gomes, J. Qu, G. A. Rome, S. M. Baumann, E. Ertekin, and E. S. Toberer, Native defect engineering in $CuInTe_2$, Chem. Mater. **33**, 359 (2021).